京都大学防災研究所年報 第 63 号 B
DPRI Annuals, No. 63 B, 2020

Strong Motion Simulation for the 1944 Tonankai Earthquake Based on the Statistical Green's Function Method and Stochastic Representation of Complex Source Process

Eri ITO, Kenichi NAKANO (1), Haruko SEKIGUCHI, and Hiroshi KAWASE

(1) HAZAMA-ANDO CORP., Tsukuba, Japan

Synopsis

The precise evaluation of source, path, and site terms in a broad-band frequency range is indispensable for quantitative prediction of strong motions. We have conducted the generalized spectral inversion on strong motions in Japan to delineate both the spectral amplitude and phase characteristics for statistical Green's functions. To predict mega-thrust earthquakes, we also need to model a kinematic source with stochastic representation of slip and rupture velocity on the fault surface. In this preliminary study we first report the basic features of our statistical Green's functions used for summation. We then show how to construct a kinematic source with distinctive strong-motion generation areas with spatially random slip and rupture velocity variations. After the summation we found that the PGAs and PGVs of synthetics for the M_w8.0 1944 Tonankai earthquake are in good agreement with those of the empirical formula. We see relatively small effects of the random slip distribution.

Keywords: Mega-thrust earthquake, Tonankai earthquake, Generalized Spectral Inversion, Stochastic source, statistical Green's function method

1. Introduction

The quantitative strong motion prediction with a source- and site-specific scheme is very important for mitigation of earthquake disaster and seismic design of important structures. It is especially true in Japan where large mega-thrust earthquakes are expected to occur within coming 30 years along the Nankai Trough on the subduction interface between the Japan Islands and the Philippine Sea Plate. Strong motion prediction in a broad-band frequency range from a large fault is not an easy task because we need to represent complex nature of source, path, and site.

There are several ways to simulate strong motions as waveforms on the surface at a target site located at an arbitrary position. One is the theoretical method in which wave generation at the source, propagation from the source to the site, and local site amplification near the site are represented by the numerical modeling of the medium and wave generation and propagation inside. In this method we need a good physical model of the medium to represent wave propagation phenomena in the whole path from the source to the target site. In other words, we need to calculate first the Green's function for a point source on the fault surface. Because of the limit both on the computational resource and the accuracy of geophysical model that we can use, the frequency coverage of the theoretical method is usually limited in a lower frequency range below 1 Hz, although we have several recent attempts to expand the limit up

to 5 Hz (e.g., Roger et al., 2019).

Another method is an empirical one in which we use observed ground motions of a small earthquake as a substitute of the Green's function and sum up all the contributions from the elemental sources on the fault surface. It is called the empirical Green's function method (EGF). EGF has been proved to be good at reproducing the observed mainshocks if we use good aftershock records (e.g., Kamae and Irikura, 1998; Kamae and Kawabe, 2004).

If there are no appropriate small earthquake records to be used as an empirical Green's function, we first generate synthetic waveforms from a lot of small earthquakes and sum up them to represent a large event. It is called the statistical Green's function method (SGF). SGF is very useful for prediction of strong motions for the events that have not occurred yet or those that had not been observed by the strong motion instruments.

Because the frequency range for the theoretical method with coherent nature is limited to the lower end, usually below 1 Hz or lower, whereas the valid range for EGF or SGF with inherent nature of stochasticity should be higher than that, a hybrid scheme for a theoretical method with EGF or SGF are used naturally, as has been used in the current national project for strong motion predictions with specific sources (J-SHIS, 2020).

However, after the deployment of the dense national strong motion observation networks, namely K-NET, KiK-net, and JMA Shindokei network, a significant number of data has been accumulated, and therefore, we can use these data to construct a model of SGF in a broad-band frequency range. As long as we can generate the SGF for an arbitrary size of a small earthquake at an arbitrary location in a frequency range of interest, namely from 0.1 Hz to 20 Hz, we need not to use a hybrid scheme (e.g., Ito and Kawase, 2001; Ho and Kawase, 2007). This means that we do not need to spend our time to construct a physical model for the complex earth.

Thus, we have been analyzing these strong motion data in Japan by using the generalized spectral inversion technique (GIT, Andrew, 1986; Iwata and Irikura, 1988) to delineate statistical properties of the three major terms, namely, the source term, the path term, and the site term (Kawase and Matsuo, 2004; Nakano et al., 2015; Nakano, 2020). The novelty of our approach is that the hypothesized (i.e., deconvolved) seismological bedrock spectra at a reference site, YMGH01, are used as a reference to calculate site amplification factors at all the observed sites. Such a separation of observed spectra into three major terms is sufficient to generate SGF at these sites.

However, strong motion simulations for a mega-thrust earthquake on the subduction zone need complex source representation for realistic synthetics. Before the 2011 Off the Pacific Coast of Tohoku earthquake of M_w9.0 we do not have a concrete picture of the source complexity. The source inversions of this earthquake provided us a lot of information useful for the source representation indispensable for broad-band simulations of future earthquakes (e.g., Asano and Iwata, 2012; Kurahashi and Irikura, 2013). Therefore, whenever we predict strong motions for a mega-thrust earthquake after Tohoku event, we must reflect important characteristics on the complex nature of its fault rupture process.

Considering the fact that these mega-thrust events along the Nankai Trough have been occurring periodically (e.g., Ando, 1975), we need to learn from previous experiences as much as we can. Before the nation-wide deployment of strong motion networks, however, delineation of the complex rupture process during the past events are quite difficult because we do not have sufficient constraints from observations. To this end, we would like to use damage statistics of wooden houses, not the seismic intensity, as the physical constraints for the source complexity based on the simulated (reproduced) ground motions together with the structural damage prediction model (e.g., Nagato and Kawase, 2004).

In what follows we first introduce fundamental characteristics of the SGF derived from the GIT applied to the strong motion records by K-NET, KiK-net, and the JMA Shindokei network (Nakano et al., 2015; Nakano, 2020). Then, we introduce a stochastic representation in a kinematic source model for a complex rupture scenario of Tonankai earthquake with the size of 1944 event based on the strong-motion generation areas (SMGAs) with spatially-random perturbation in both slip and

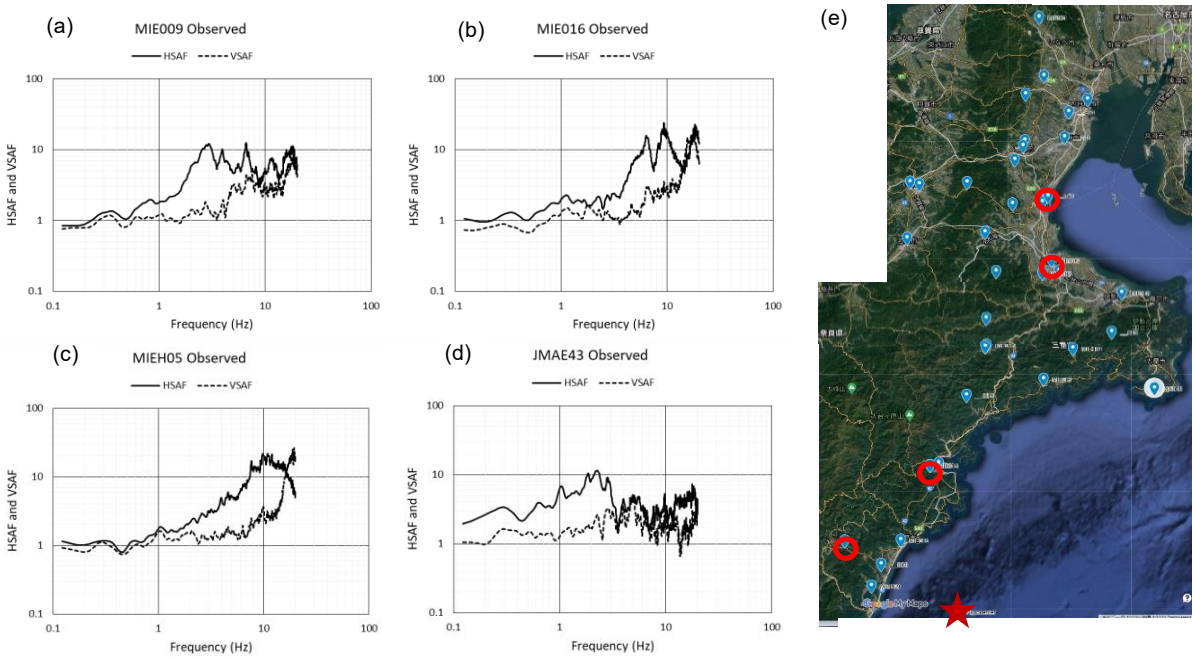

Fig. 1 Site amplification factors (HSAF and VSAF) extracted from the S-wave portions of records observed at K-NET, KiK-net, and JMA Shindokei network used in the SGF simulation (Nakano et al., 2015) at four sites in Mie Prefecture. A map on the right shows their locations, with a rupture initiation point (★).

rupture velocity. Finally, we calculate synthetic waveforms in the vicinity of the fault area and confirm their appropriateness in term of their average characteristics in the strength indices. We will use these acceleration synthetics to simulate observed damage of wooden houses during the 1944 Tonankai earthquake.

2. Statistical Green's function

2.1 Outline of GIT

In this section we briefly introduce the observed horizontal site amplification factor (HSAF) and vertical one (VSAF) derived from GIT (Nakano et al., 2015; Nakano, 2020). Here we only introduce their basic aspects since we are using their results as a starting point.

Based on the ordinary non-parametric GIT concept, the S-wave Fourier spectrum of the horizontal motion, F_{S_ij}, of earthquake i observed at site j would be decomposed into the common logarithmic sum of the source term S_{S_i}, the path term P_{S_ij}, and the horizontal site amplification factor at site j, H_{S_j}, as shown in the following equation:

$$\log F_{S\_ij} = \log S_{S\_i} + \log P_{S\_ij} + \log H_{S\_j} \quad (1).$$

Likewise, the S-wave Fourier spectra of the vertical motion, G_{S_ij}, is decomposed into the following equation:

$$\log G_{S\_ij} = \log S_{S\_i} + \log P_{S\_ij} + \log V_B H_B R + \log V_{S\_j} \quad (2).$$

These equations assume that ground motion is propagated as S-waves until reaching the seismological bedrock immediately below the observation site and then a part of the energy of S-waves is converted to P-waves, which are observed as vertical motion on the ground surface. Here, V_{S_j} is the vertical site amplification factor for site j, whereas the third term in equation (2), $V_B H_B R$, is a coefficient for converting horizontal (S-wave) amplitude into vertical (P-wave) amplitude, and theoretically it corresponds to the inverse of the horizontal-to-vertical amplitude ratio of the incident wave at the seismological bedrock, which would be equal to the square-root of the ratio of the P-wave velocity to the S-wave velocity on the seismological bedrock in the diffuse field regime (e.g., Kawase et al., 2011; Nagashima et al., 2014; Ito et al, 2020). This coefficient is needed because the main portion of wave energy consists of the S-waves propagated and scattered through the medium from the hypocenter to the point on the seismological bedrock

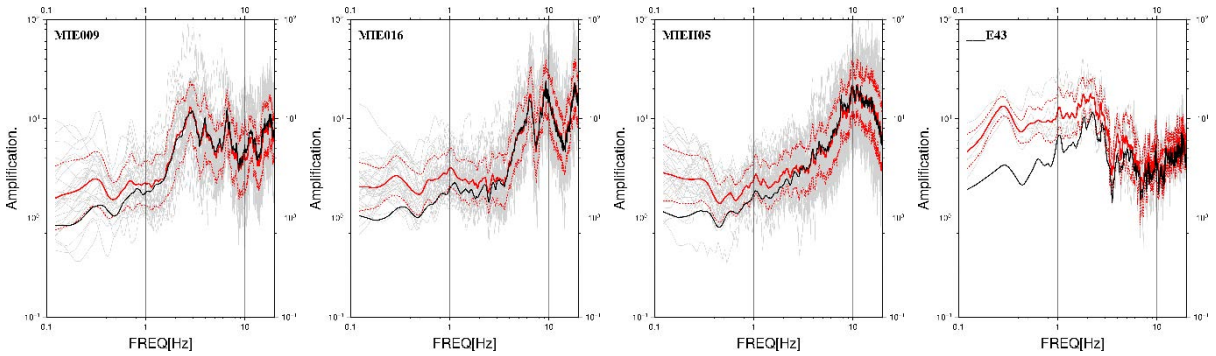

Fig. 2 HSAFs for the S-wave portion shown in Fig.1 (black lines) and those for the whole duration (red lines), together with its deviations (red dotted lines) and individual ones (Nakano, 2020).

immediately below the site, while V_{S_j} represents the vertical (P-wave) amplification factor from the seismological bedrock to the surface. Please note that HSAF and VSAF are the general terms referring to the site amplifications in the horizontal and vertical directions, while H_{S_j} and V_{S_j} are the specific terms derived from GIT.

We restricted events and sites with JMA magnitude $M_{JMA} \geq 4.5$; source depth $\leq$ 60 km; hypocentral distance $\leq$ 200 km; peak ground acceleration $\leq$ 2 m/s^2; and number of observation sites triggered simultaneously for one event $\geq$ 3. These selection criteria resulted in 77,213 event-station pairs at 2,105 sites for 967 events. Only a relatively short duration of acceleration record from the onset of the S-wave is analyzed (5 s if $4.5 < M_{JMA} \leq 6$; 10 s if $6 < M_{JMA} \leq 7$; 15 s if $7 < M_{JMA} \leq 8$). A Parzen window of 0.1 Hz is used for a minimum level of smoothing. As mentioned above, the most important feature of their GIT is that they determined the S-wave velocity structure at the reference site using the transfer function (the spectral ratio and the phase difference) between the surface and the borehole 200 m below and that the observed Fourier spectra on the surface were deconvolved to obtain the hypothesized outcrop spectra on the seismological bedrock with an S-wave velocity of 3,450 m/s. Nakano et al. (2015) and Nakano (2020) successfully separated the source spectra and path terms as evidenced by their correspondence to the ω^{-2} source spectra shapes and Q values similar to the previous studies in Japan.

Fig. 1 shows examples of the separated HSAF and VSAF at four representative sites in Mie Prefecture. We can see significant differences from site to site in HSAF. The amplitude and its fluctuation of VSAF is much smaller than HSAF, especially below 3 to 7 Hz. That is why the earthquake horizontal-to-vertical spectral ratio, eHVSR, tends to be similar to HSAF until the fundamental peak frequency of VSAF. However, to get HSAF from eHVSR, we need to correct VSAF, as recently proposed by Ito et al. (2020). Please note that VSAFs shown in Fig.1 are the site amplification factors of the vertical component with respect to the horizontal component on the seismological bedrock, referred to as VSAF* in Ito et al. (2020). Because we are specifically predicting the S-wave spectra radiated from the source, we need to use the relative amplification factors of the vertical component to the S-wave input on the seismological bedrock.

2.2 WSR to account for basin effects

One of the novelties of our SGF based on GIT is the back calculation of the site factors for the whole duration. When our target sites are located within a sedimentary basin, we see additional amplification due to the basin-induced surface waves generated at the edge of a 2D or 3D basin (e.g., Bard and Bouchon, 1980; Kawase and Aki, 1989; Kawase, 2003). They are quite significant in the lower frequency range below 1 Hz, especially inside soft and large basins. However, if we use directly the whole duration of motion as the target of the GIT analysis, the resultant attenuation would be totally distorted. When we use the whole duration, the Fourier spectra inside a basin but away from the source become larger than those closer to the source but outside of a basin, we cannot see any attenuation in proportion to the distance, and therefore, we will have negative Q values.

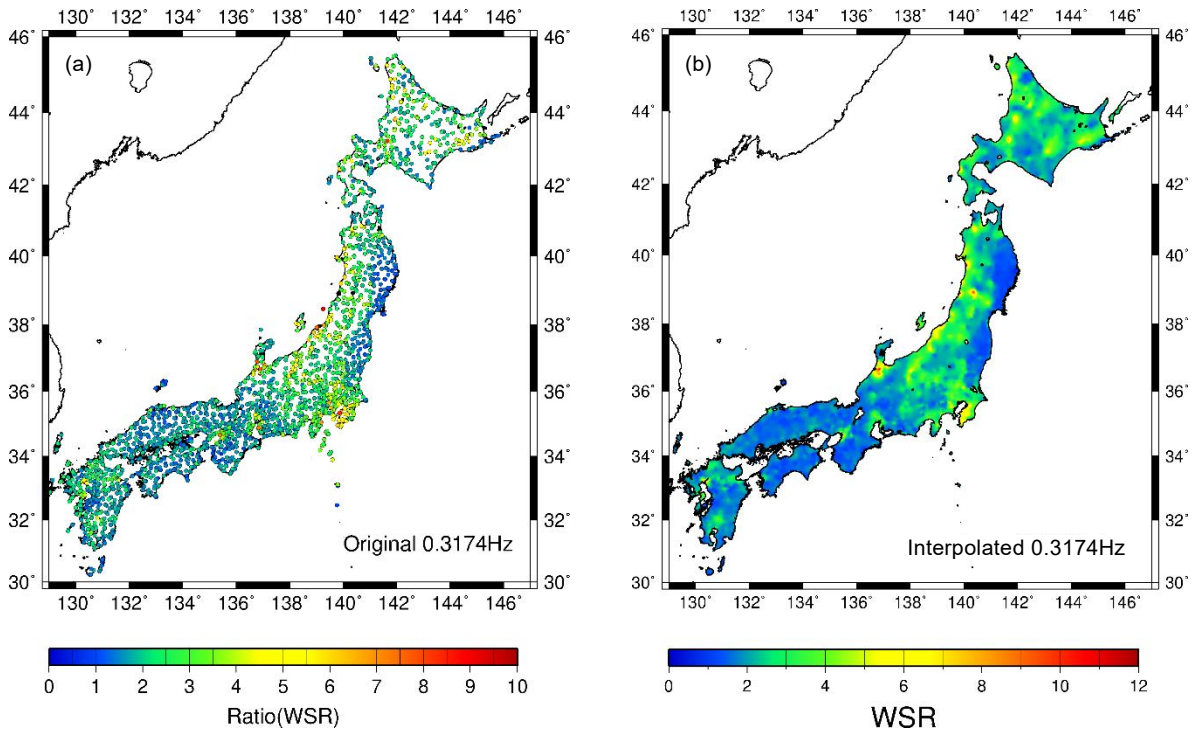

Fig. 3 Comparison of (a) WSRs calculated from the observed data and (b) those interpolated to higher spatial resolutions (Nakano, 2020).

To account for the effects of the basin-induced surface waves inside sedimentary basins, Nakano et al. (2019) and Nakano (2020) proposed to use an empirical ratio called the whole-wave-to-S-wave ratio (WSR), where the spectral ratios of the whole duration with respect to the S-wave portion with relatively short duration (5 to 15 s as mentioned above) are averaged over all the observed events at a site. They found that the WSR tends to be close to 1 irrespective of frequency for a site on a hard rock, whereas it can easily exceed 10 in the lower frequency range for a site inside a soft sedimentary basin. Even for such a site, WSR will converge to 1 in the frequency range higher than 1 to 2 Hz. In Fig. 2 HSAFs for the S-wave portions and those for the whole duration are compared. MIE009, MIE016, and MIEH16 show normal characteristics of the sites outside of a sedimentary basin, whereas JMAE43 shows those inside a basin. Simply WSR is the spectral ratios between red and black lines in this figure.

Because the spatial variation of WSR at one specific frequency highly correlates with that of the basin depths, as seen in Nakano et al. (2019), Nakano (2020) proposed a scheme to interpolate WSRs to make it possible to calculate a scenario-type hazard map with much higher spatial density (in 250 m grid) than those of strong motion observation sites. The interpolation scheme utilized the surface function of GMT (Smith and Wessel, 1990), together with the code developed by Renka (1999). This WSR correction is a simple, empirical way to account for the additional amplifications due to soft sedimentary basins. In Fig. 3 we plot the original WSRs for HSAF all over Japan and those interpolated based on the scheme proposed by Nakano (2020) at 0.3174 Hz. We can see how the WSR corrections are significant in the lower frequency range inside the large sedimentary basins, especially in the Eastern Japan in the east of the Itoigawa-Shizuoka tectonic line.

2.3 Tgr modeling

To calculate synthetic waveforms for small to moderate-sized earthquakes as SGFs, we need to specify their phase information or envelope functions to constrain the time-varying characteristics of synthetic SGFs. It is desirable to use phase spectral information because we can account for the frequency dependence of the envelope shape. Thus we follow the procedure of Nakano (2020) to model the group delay time, t_{gr} as:

$$t_{gr} = \frac{d\emptyset(\omega)}{d\omega}, \quad (3)$$

where

$$\emptyset(\omega) = \tan^{-1}(I(\omega)/R(\omega)), \quad (4)$$

and

$$t_{gr} = \frac{R(\omega)\cdot I(\omega)' - R(\omega)\prime\cdot I(\omega)}{R^2(\omega)+I^2(\omega)} \quad (5).$$

Then we can model the average and variance characteristics of t_{gr} for the whole duration of observed record $\mu(f)$ and $\sigma(f)$ as

$$\mu\_ij(f) = \mu^{Source\_i}(f) + \sum_k \mu_{ij}^{pass}(f)\cdot X_{ij}^{1.9} + \mu^{Site\_j}(f), \quad (6)$$

$$\sigma\_ij(f) = \sigma^{Source\_i}(f) + \sum_k \sigma_{ij}^{pass}(f)\cdot X_{ij}^{1.9} + \sigma^{Site\_j}(f), \quad (7)$$

for the i-th source observed at j-th site.

We show examples of the site terms in equation (6) in Fig.4 for the same sites shown in Figs. 1 and 2. Only JMAE43 site shows significantly longer durations (rate arrivals), especially in the lower-frequency range.

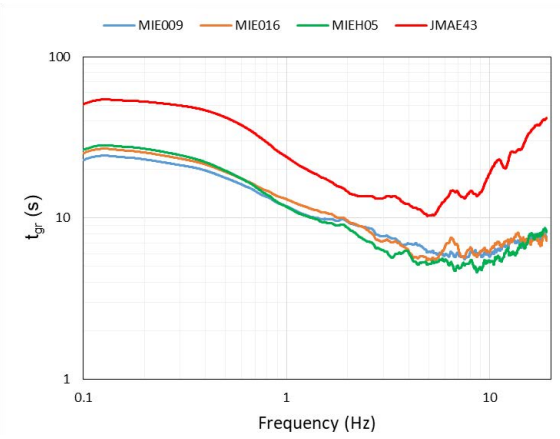

Fig. 4 Site factors for the average t_{gr} in equation (6) extracted by GIT for the whole duration of records.

3. Stochastic Source Model

A broadband heterogeneous source model is generated for a plate boundary earthquake along the Nankai Trough by introducing fractal heterogeneity into a characterized source model consisting of a background region and a strong-motion generation region.

The gross ruptured area (i.e., the assumed fault plane) of the fault map of the Central Disaster Management Council (CDMC, 2003) is projected on the upper surface of the Philippine Sea plate of the Japan Integrated Velocity Structure Model (JIVSM; Koketsu et al., 2012) and adjusted the size to be compatible to the fault size of CDMC and to be able to include the strong-motion generation areas (SMGAs) of the Cabinet Office (2015). For the assumed SMGAs here, their areas, moments, stress parameters, rise time, and center positions are adopted from those values by the Cabinet Office (2015) as the basic model (Table 1). However, the shape of the SMGA is assumed to be circular, unlike those of the Cabinet Office (2015). We assumed as such because we want to use an automatic generation system for a large number of parametric studies with various locations and areas of SMGA in future. The parameters of the background region of the basic model are based on CDMC (2003). The amount of the average slip is calculated from the total moment and the fault area, similar to the method used by CDMC (2003).

The broadband source heterogeneity is calculated by randomly adding heterogeneity from about one half of the SMGA areas to several km^2 in size to the basic source parameter distribution consisting of the background and SMGAs, as described in Sekiguchi and Yoshimi (2010). The amplitude of fluctuation is proportional to the size of heterogeneity. We adjust the power of the fall-off in the spatial distribution of the slip heterogeneity is equal to the value obtained by Mai and Beroza (2002), that is, -1.75. The stress parameter distribution was given in proportion to the variation of the slip distribution. The rupture velocity distribution was started from a uniform distribution of 2.7 km/s and a constant amount of variation regardless of the area of the inhomogeneous patch were added and finally adjusted so that the standard deviation of the spatial variation is equivalent to the level obtained by Miyakoshi and Petukhin (2005) in their analysis of the source-inversion model. The distribution of rupture initiation times at an arbitrary point on the fault was obtained through the wave propagation analysis based on an ordinary two-dimensional finite difference method.

Fig. 5 shows the assumed shape of the whole

Table 1 Fault parameters for the 1944 Tonankai earthquake (After CDMC, 2003)

	Area [km^2]	Moment [Nm]	Mw	Stress parameter [MPa]	Rise time [s]	Center Longitude	Center Latitude
SMGA 1	618.1	1.9e20	7.4	30.0	4.6	135.75	33.20
SMGA 2	619.6	1.9e20	7.4	30.0	4.6	134.90	33.70
SMGA 3	906.8	3.4e20	7.6	30.0	5.6	134.00	33.10
SMGA 4	906.3	3.4e20	7.6	30.0	5.6	133.30	32.70
Background				2.4	10.0		

ruptured area and the SMGAs, whereas Fig. 6 shows randomized rupture velocity on the stochastic fault model used for strong motion simulations, the results of which will be shown in the next section.

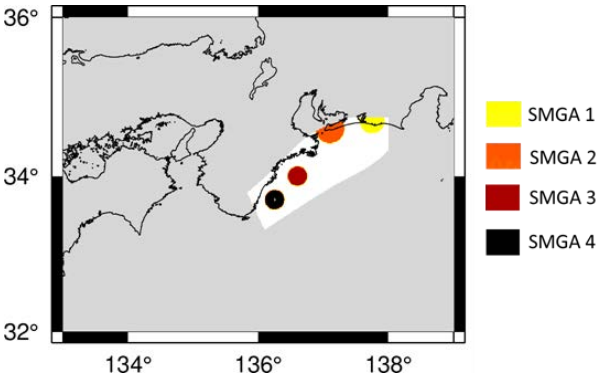

Fig. 5 Predefined strong motion generation areas (SMGAs) and the whole fault area for the simulation of 1944 Tonankai earthquake.

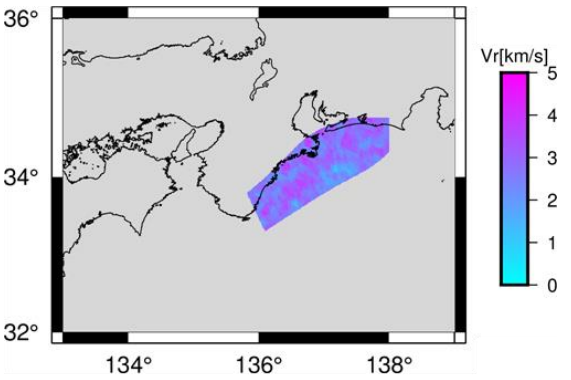

Fig. 6 Randomized rupture velocity on the stochastic fault model of 1944 Tonankai earthquake.

4. Results

4.1 Scenario with variable slip and constant rupture velocity (CASE1)

A model with variable slip and constant rupture velocity (CASE1) yields strong motion synthetics with PGAs and PGVs that correspond well to the empirical relationship by Morikawa and Fujiwara (2013). As for the deviation, the PGAs are overestimated a little bit while the PGVs are underestimated a little bit. At JMAE43, which is in a basin, the peak of the response spectra are within 0.5~2 second. At MIE016, which is located near the fault, the response spectra are larger than ones of the strong ground motion by Ministry of Construction Notice in the short period at JMAE43.

Fig. 7 shows attenuation of PGA & PGV in CASE1. Red circle shows PGA and PGV at each site, while the black line shows the empirical relationship from Morikawa and Fujiwara (2013) and the black dotted line shows its standard deviation. Fig. 8, 9 10 show acceleration waveforms, Fourier spectra, and response spectra at JMAE43, respectively, which Fig. 11, 12 and 13 show those at MIE016, respectively. In Fig. 7, the horizontal axis is the minimum distance from the fault, and the vertical axis is PGA in the upper graph and PGV in the lower graph. In Fig. 8 and Fig. 11, the horizontal axis is time and the vertical axis is acceleration. In Fig. 9 and Fig. 12, the horizontal axis is frequency and the vertical axis is Fourier spectra. In Fig. 10 and Fig. 13, the horizontal axis is period and the vertical axis is response spectra.

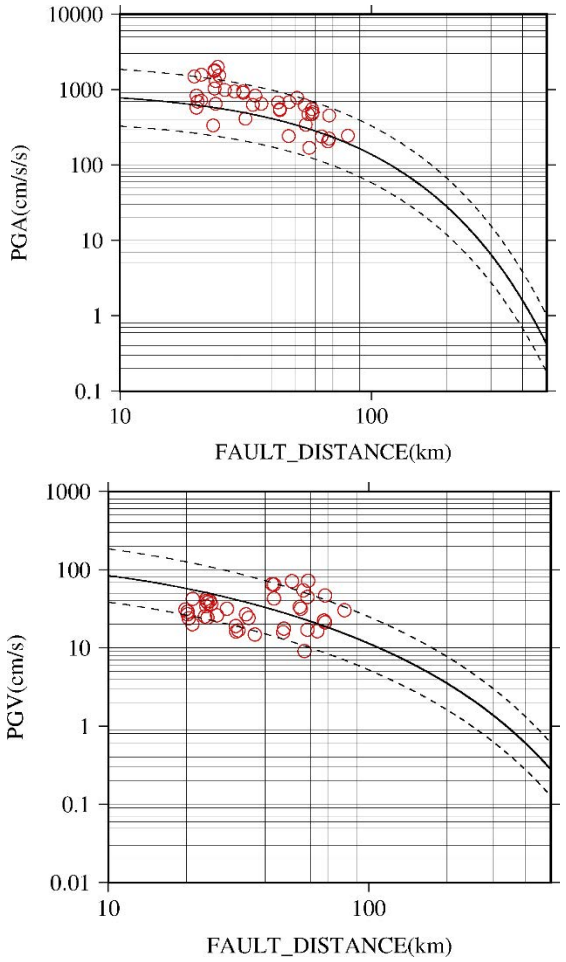

Fig. 7 Attenuation of PGA & PGV in CASE1

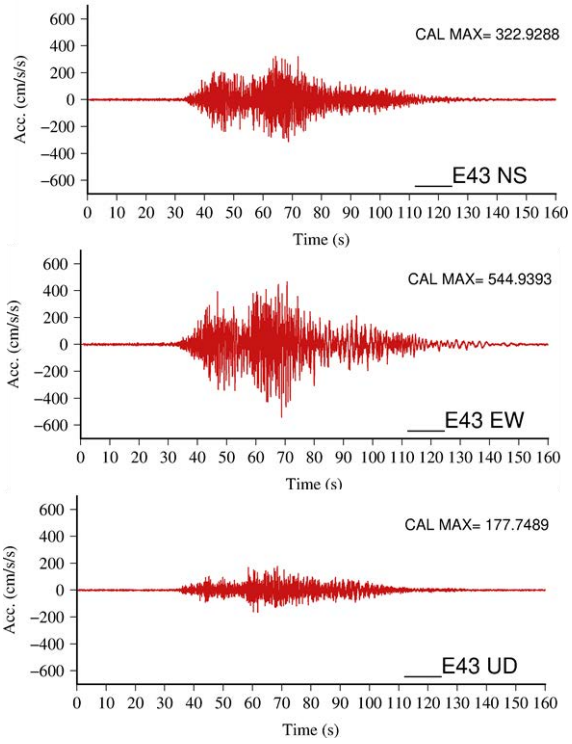

Fig. 8 Acceleration waveforms at JMAE43 in CASE1

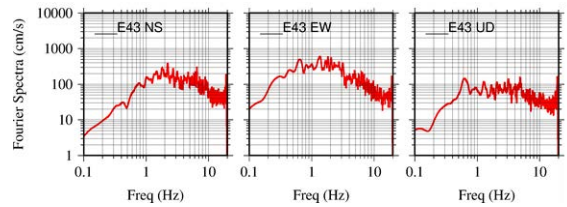

Fig. 9 Fourier spectra at JMAE43 in CASE1

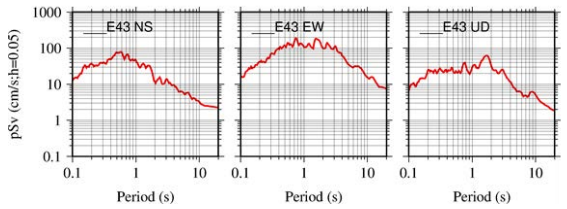

Fig. 10 Response spectra at JMAE43 in CASE1

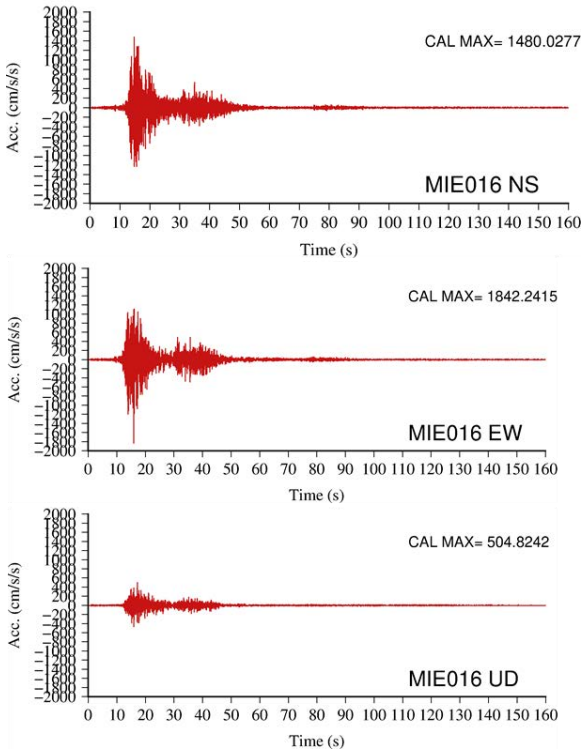

Fig. 11 Acceleration waveforms at MIE016 in CASE1

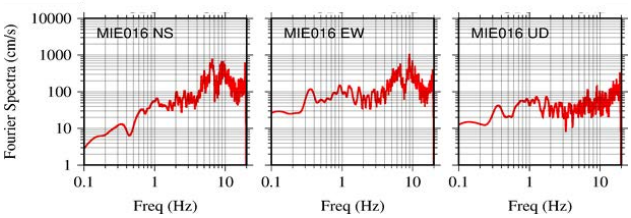

Fig. 12 Fourier spectra at JMAE43 in CASE1

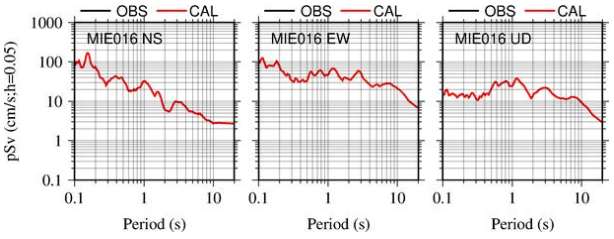

Fig. 13 Response spectra at JMAE43 in CASE1

4.2 Scenario with constant slip and constant rupture velocity (CASE2)

A model with constant slip and constant rupture velocity (CASE2) yields strong motion synthetics with PGAs which correspond with the empirical relationship, but the PGVs are lower than the empirical relationship at sites near the hypocenter. At MIE016, the Fourier spectra are about the half of the one in CASE1 within 0.3~0.4Hz, where the difference between them is the most significant. The response spectra are slightly smaller for CASE2 in almost every period band, with the smallest being about one-half to two-thirds of that of CASE1 at 0.4 to 0.5 s.

Fig. 14 shows attenuation of PGA & PGV in CASE2.Red circle shows PGA and PGV at each site, while the black line shows the empirical relationship from Morikawa and Fujiwara (2013) and the black dotted line shows its standard deviation. Fig. 15,16 and 17 show acceleration waveforms, Fourier spectra, and response spectra at MIE016. We don't show the results at JMA E43, the differences between CASE1 and CASE1 are not so clear.

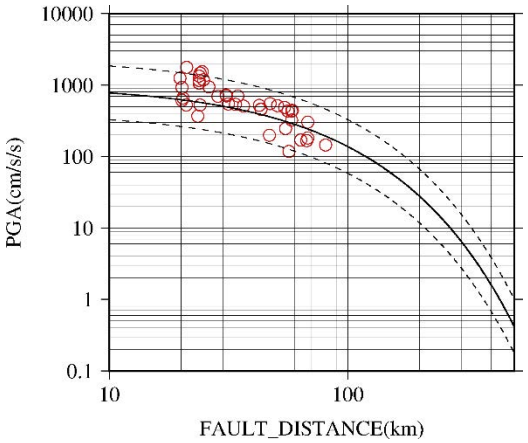

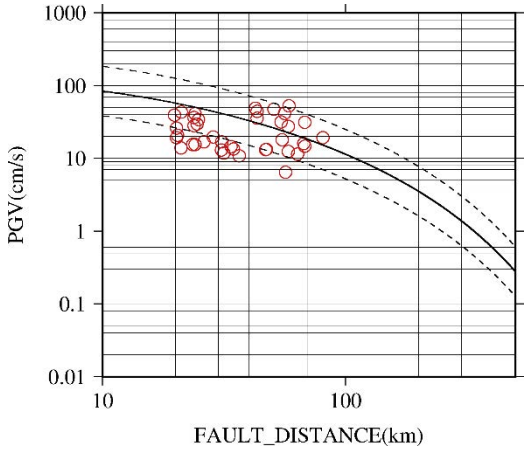

Fig. 14 Attenuation of PGA & PGV in CASE2

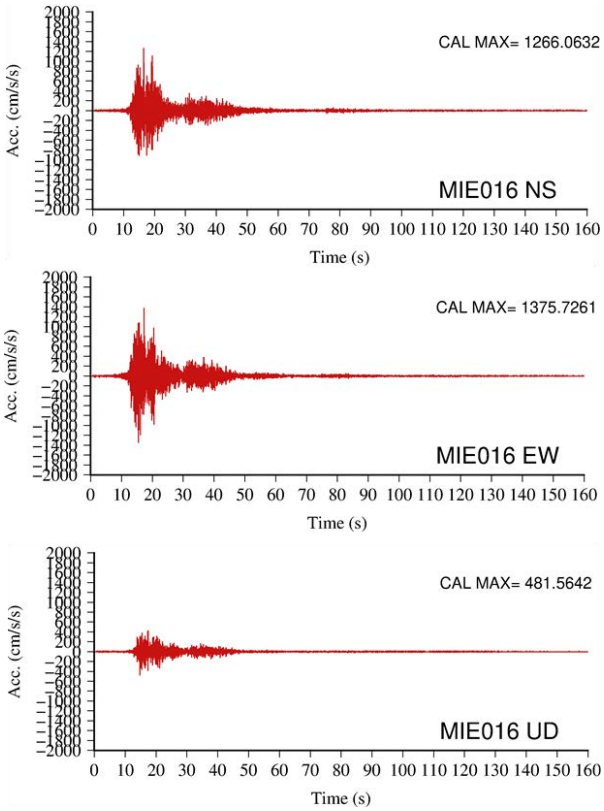

Fig. 15 Acceleration waveforms at MIE016 in CASE2

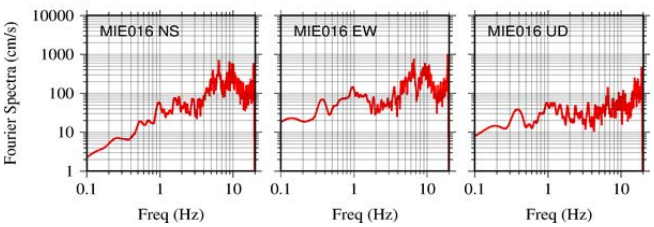

Fig. 16 Fourier spectra at MIE016 in CASE2

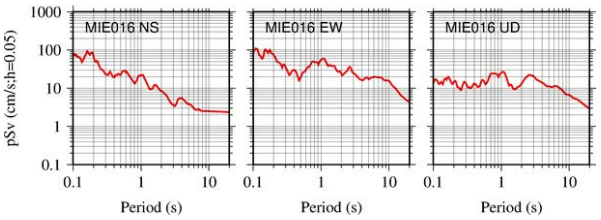

Fig. 17 Response spectra at MIE016 in CASE2

4.3 Scenario with variable slip and variable rupture velocity (CASE3)

A model with variable slip and variable rupture velocity (CASE3) yields strong motion synthetics with PGAs and PGVs that corresponds well to the empirical relationship. In particular, the PGAs show more correspondence with the empirical relationship at sites near the hypocenter than those of CASE1, where the speed of rupture propagation was held constant. In the Fourier spectra, although there are some differences in each frequency, they are at the same level on average. The response spectrum also differs in some periods, but the overall response spectrum is almost the same.

Fig. 18 shows attenuation of PGA & PGV in CASE3. Red circle shows PGA and PGV at each site, while the black line shows the attenuation curve from Morikawa and Fujiwara (2013) and the black dotted line shows its standard deviation. Fig. 19,20 and 21 show acceleration waveforms, Fourier spectra, and response spectra at MIE016. We don't show the results at JMA E43, the differences between CASE1 and CASE1 are not so clear.

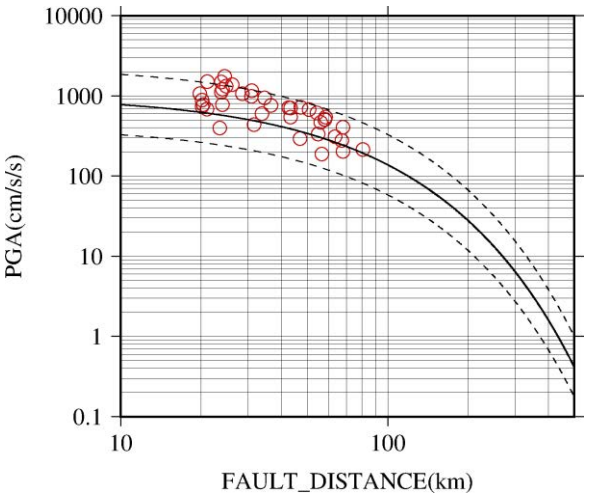

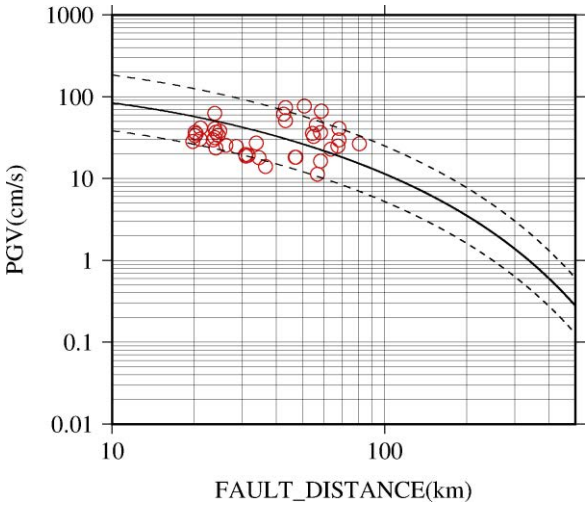

Fig. 18 Attenuation of PGA & PGV in CASE3

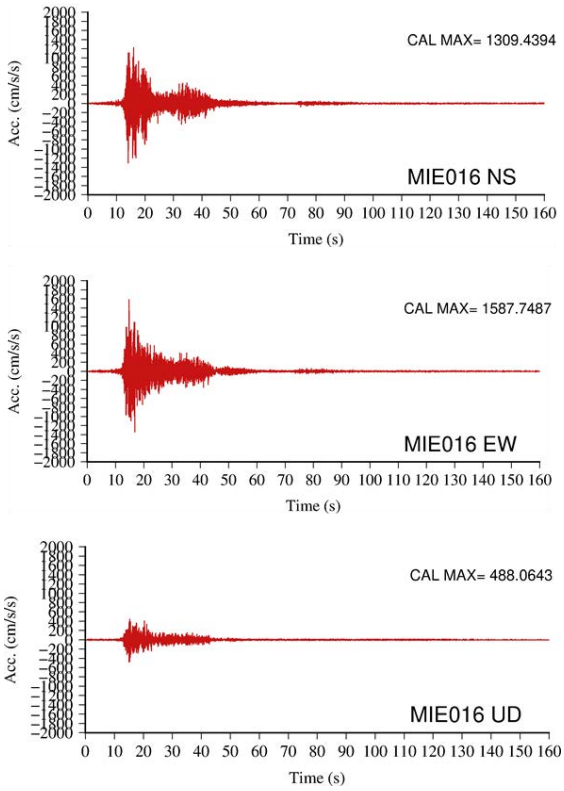

Fig. 19 Acceleration waveforms at MIE016 in CASE3

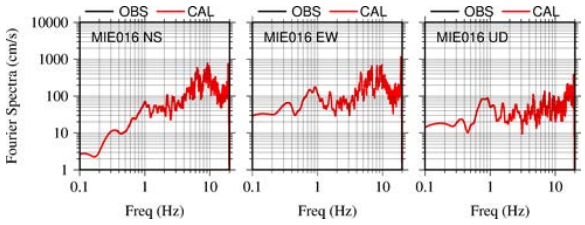

Fig. 20 Fourier spectra at MIE016 in CASE2

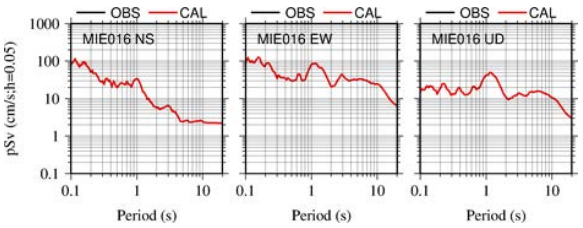

Fig. 21 Response spectra at MIE016 in CASE2

5. Discussion

5.1 Effects of slip variation on PGA and PGV

As shown in the Sections 4.1 and 4.2, we can see relatively small difference between the simulated synthetics from CASE1 and those from CASE2 at a selected site (MIE016) near the hypocenter. The difference reflects the effect of the slip variation on the fault. We need to check if it is a universal observation at all the sites analyzed.

Fig. 22 shows comparisons of PGA and PGV at all 40 sites in Mie Prefecture. It is clear that the PGA from a model with spatial slip variations (CASE1) tends to be slightly higher than the PGA from a model without spatial slip variation (CASE2). For a smooth slip model (CASE2) we see about 15% reduction in PGA in comparison to a variable slip model. On the other hand, the PGVs from a model with spatial slip variations (CASE1) tend to be apparently higher than the PGVs from a model without spatial slip variation (CASE2). For a smooth slip model (CASE2) we see about 25% reduction in PGVs in comparison to a variable slip model.

These observations may come from the fact that the PGA is primarily controlled by the high frequency component, where the random pulses will overlap in the superposition from each elemental source so that it is difficult to see the effects by the slip variations in individual elements with the size of 5km x 5km, whereas the PGV is controlled in the intermediate frequency component (0.5 to 5 Hz) so that coherent interferences of waves from different elemental sources are taking place so that we can see stronger effects of the slip variation. In our current simulations, we do not assume any spatial fluctuation of the stress drop in the elemental sources which controls the high-frequency radiation level. It may be necessary to consider the spatial fluctuation of the stress drop to understand how it affects the high frequency range of the synthetic waveforms in the future.

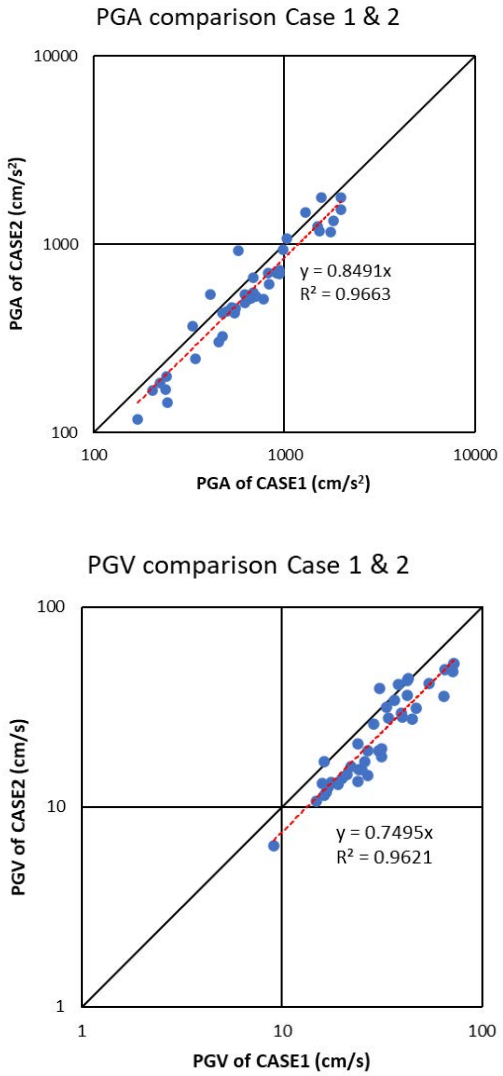

Fig. 22 Comparisons of PGA and PGV for the calculated synthetics with slip variations (CASE1) and without slip variations (CASE2).

5.2 Effects of rupture velocity variation on PGA and PGV

As shown in the Sections 4.1 and 4.3, we can see a minor effect between the simulated synthetics from CASE1 and those from CASE3 at a selected site near the hypocenter. The difference reflects the effect of the rupture velocity variation on the fault. We need to check if it is a universal observation at all the sites analyzed.

Fig. 23 shows comparisons of PGA and PGV for CASE1 and CASE3 at all 40 sites in Mie Prefecture. It is clear that both the PGAs and PGVs show almost 1:1 correspondence. Although the averaged

difference is only 5% for PGA, it is noticeable that higher PGA values in the vicinity of the hypocenter tend to become smaller in CASE3 than in CASE1. This phenomenon can be interpreted as the result of the incoherent rupture directivity in CASE3, in comparison to the coherent rupture directivity in the near-fault regions. When the rupture velocity fluctuates from one elemental source to the other, the forward rupture directivity could become weaker than the constant rupture velocity case.

Please note that these values inevitably fluctuate from site to site even for the same parameter case since we include random phase component in the elemental-source waveform generation.

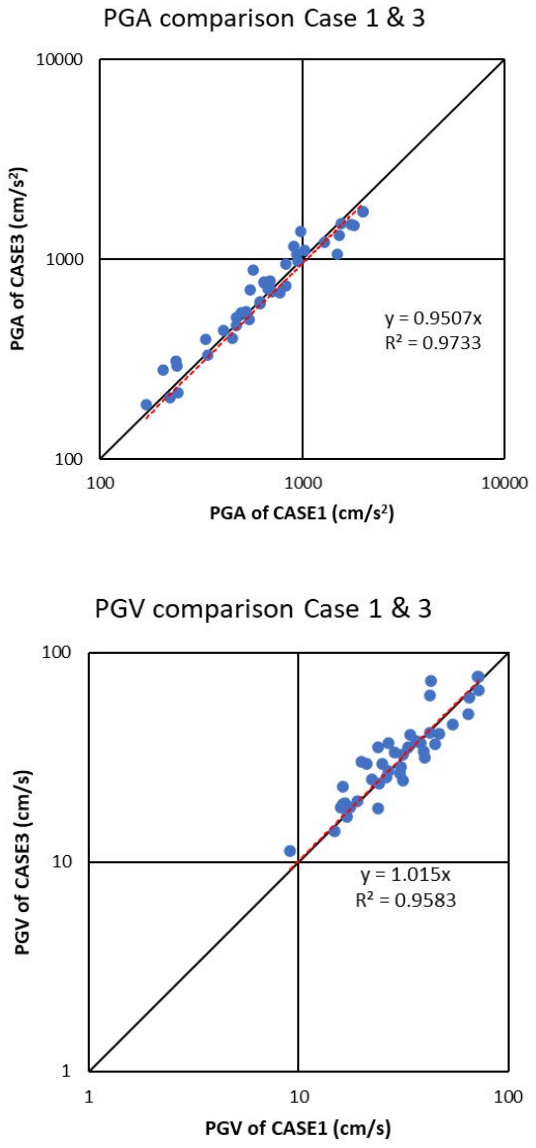

Fig. 23 Comparisons of PGA and PGV for the calculated synthetics with rupture velocity variations (CASE1) and without rupture velocity variations (CASE3).

5.3 Effects of nonlinearity on PGA and PGV

As seen in the simulation results in Chapter 4, we have high PGV areas inside the Ise Plain where a strong site amplification in the lower frequency range is observed (Fig. 4). When a strong input of seismic motion is impinged to thick, soft sediments, soil nonlinearity is taking place and we will have a smaller amplitude in the site amplification factor than the linear one (amplitude degradation), and a peak frequency shift. Nakano (2020) proposed two methods to account for the soil nonlinearity in his SGF code; one with only the amplitude degradation, and the other with both the amplitude degradation and the peak frequency shift. In this report we only consider the amplitude degradation for simplicity.

The amplitude degradation curve that Nakano (2020) proposed is based on the collected 174 high PGA and PGV records, together with the Vs30 values (the so-called time-averaged S-wave velocity of top 30 m) at their observation sites. The method follows the one proposed by Yamaguchi and Midorikawa (2014), in which the pseudo-effective shear strain γ'_{eff} is defined as:

$$\gamma'_{eff} = 0.4 \cdot \mathrm{PGV}/Vs30. \tag{8}$$

Then the spectral amplitude degradation $G'(f)$ is modeled as:

$$G'(f) = \alpha\left(f, \gamma'_{eff}\right), \tag{9}$$

$$log_{10}\alpha\left(f, \gamma'_{eff}\right) = a(f) \times \left(log_{10}\gamma'_{eff} - log_{10}\gamma'_{eff\_0}\right) \tag{10}$$

in which $a(f)$ is the regression coefficient for each frequency using a linear function with respect to γ'_{eff} and $\gamma'_{eff\_0} = 3.0 \times 10^{-4}$ is the threshold strain level of the linear regime assumed a priori. The regression coefficient $a(f)$ is shown in Fig. 24 (not as a function of frequency but period T=1/f for comparison with Yamaguchi and Midorikawa, 2014). Nonlinearity will emerge as stronger amplitude degradation in the frequency range between 1 and 10 Hz.

Fig. 25 shows comparisons of PGA and PGV for

CASE1 and CASE1NL calculated by using the spectral nonlinearity shown in the above formula on top of the synthetics calculated under the same assumption as CASE1 at all 40 sites in Mie Prefecture. It shows that the PGA with nonlinearity yields the same PGA level as the linear calculation on the average. However, the PGV higher than 40 cm/s at six sites shows significant reduction. On the average PGVs with nonlinearity are 80% of PGVs with linearity as shown by the linear regression line (red dotted line), although the regression with a power law (blue dotted line) looks better fit to the data. This is rational because equation (8) shows that the PGV is the controlling parameter for the degree of nonlinearity, together with Vs30.

If that is the case, the PGAs should also be reduced at those sites with high PGVs, as the reduction shown in Fig. 24 is taking place in a broad frequency range. When we look at Fig. 25, the PGAs at the sites with strong reduction of the PGVs show also strong reduction.

On the other hand, the sites with the high PGAs near the hypocenter do not show any significant reductions in their Fourier spectra, as shown in Fig. 26 for MIE016 as an example. This is so because the effective shear strains in equation (8) at these sites were not so large due to both their smaller PGVs and their larger Vs30.

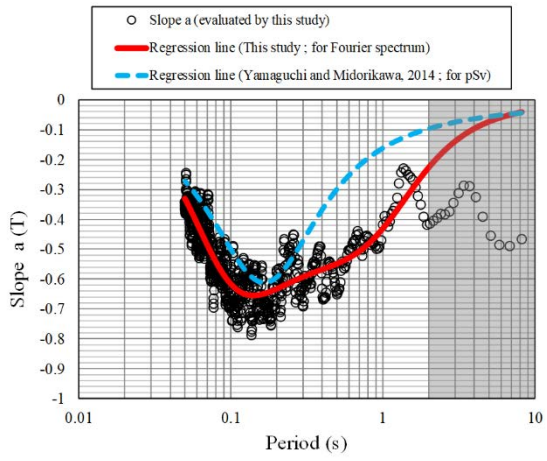

Fig. 24 Regression coefficients of nonlinearity as a function of period (1/*f*) in the site term in the form of Fourier spectra (circles and red curve as the smoothed average). In comparison, the same regression coefficients for the pseudo-velocity response spectra (pSv) by Yamaguchi and Midorikawa (2014) were also plotted (blue dotted line).

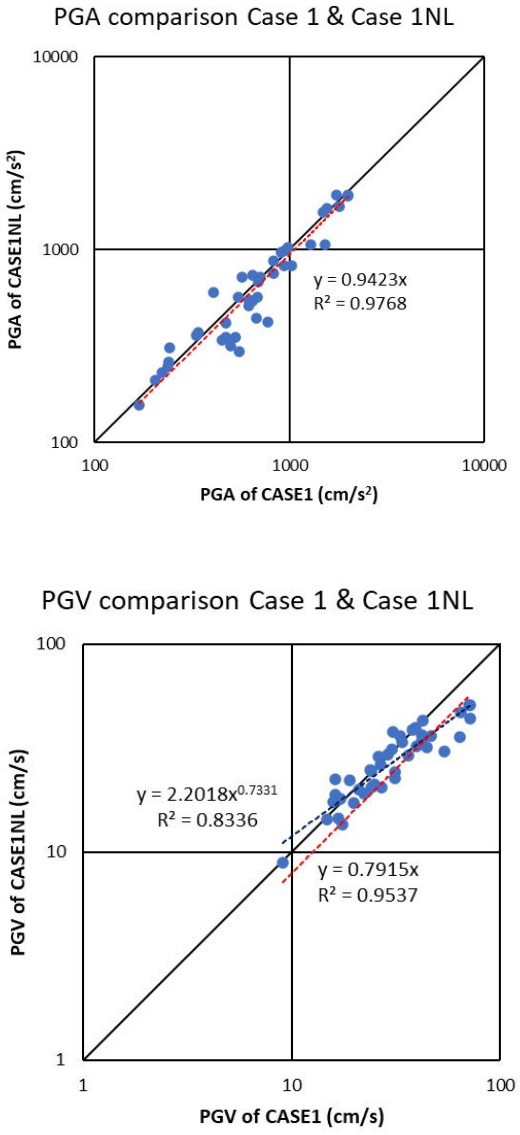

Fig. 25 Comparisons of PGAs and PGVs for the calculated synthetics without soil nonlinearity (CASE1) and with soil nonlinearity (CASE1NL).

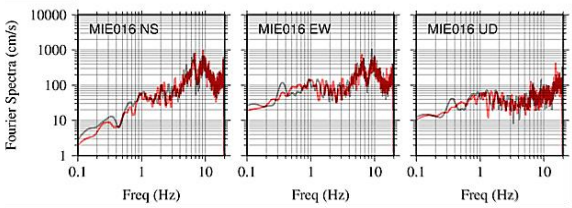

Fig. 26 Comparison of Fourier Spectra of CASE1 (in black line) with those of CASE1NL (in red line)

Considering these fundamental characteristics of the resultant soil nonlinearity, we think that the

empirical approach for soil nonlinearity correction adopted in the current implementation would be usable for large-scale prediction of strong motions as the first-order approximation. We may need further scrutiny for the degree of precision, though.

6. Conclusions

We plan to clarify the source process of the past mega-thrust earthquakes, the ground motions of which have not been recorded in the past, by adapting the simulated strong-motion waveforms to the results of the damage survey. For quantitative strong motion synthetics, we need to introduce random spatial heterogeneity in both the slip and rupture propagation velocity, in addition to the presumed strong-motion generation areas. We have developed an effective method to predict strong ground motions over a wide frequency range from 0.1 to 20 Hz by combining such a randomized source model that can represent complex rupture process on the fault and a statistical Green's function that reflects the statistical properties of small and medium-sized earthquakes inverted from a large number of strong-motion observation records in Japan. The method is applied to the 1944 Tonankai earthquake and parametric analysis is performed to investigate the effects of fluctuation in the slip and the rupture propagation velocity. The main results are summarized as follows:

1) The standard model with the random slip fluctuation but without rupture velocity perturbation (CASE1) yielded strong motion synthetics with PGAs and PGVs that correspond to the previously-proposed empirical relationship in general. A model with constant slip and constant rupture velocity (CASE2) yields strong motion synthetics with PGAs corresponding with the empirical relationship and the PGVs lower than the empirical relationship at sites near the hypocenter. A model with variable slip and variable rupture velocity (CASE3) yields strong motion synthetics with PGAs and PGVs that correspond well to the empirical relationship. The PGAs show more correspondence with the empirical relationship at sites near the hypocenter than those of CASE1.
2) Specifically looked at the deviation, their PGAs tend to be overestimated a little bit whereas their PGVs tend to be underestimated a little bit, which can be considered as the reflected site effects of the target sites used for calculation.
3) The fluctuations of the slip under the current model turned out to increase PGA by 15% and PGV in 25%.
4) The variations of the rupture propagation velocity turned out not to change both PGA and PGV significantly, probably because of the stochastic nature in the statistical Green function method adopted here. However, we see systematic reduction of PGAs in the vicinity of the hypocenter, due to the effect of the incoherent rupture in the area with strong forward directivity.
5) Empirically-modeled nonlinearity effects will reduce both PGAs and PGVs at the sites with higher PGVs and smaller Vs30, whereas those sites with higher Vs30s, where PGAs were high but PGVs were low, do not show significant reduction.

As the overall characteristics of the calculated synthetics, we found that our current implementation of the complex source model used as a broad-band kinematic source representation and the empirically-determined statistical Green function used as an elemental source of strong motions can be a viable combination for realistic broad-band (0.1 to 20 Hz) strong motion simulations without any hybrid scheme.

For future tasks, we will estimate the building damage by inputting the acceleration waveforms into the wooden building model with construction age for damage estimation, and then search the most realistic source rupture model through a large number of parametric analysis until the estimated damage ratio at each site matches the observed one.

Acknowledgements

Some of the figures presented are created by GMT (Wessel et al, 2013). Satellite image from Google Map is used in Fig.1. We use the strong motion records observed at JMA Shindokei network & K-NET and KiK-net (NIED, 2019).

References

Ando, M. (1975): Source mechanisms and tectonic significance of historical earthquakes along the Nankai trough, Japan, Tectonophysics, 27, 119-140.

Andrews, D.J. (1986): Objective determination of source parameters and similarity of earthquakes of different size, Earthquake Source Mechanics (eds. S. Das, J. Boatwright and C. H. Scholz), American Geophysical Union, Washington, D.C., 1986. doi: 10.1029/GM037p0259.

Asano, K. and Iwata, T. (2012): Source model for strong ground motion generation in the frequency range 0.1-10 Hz during the 2011 Tohoku earthquake, Earth Planets Space, Vol.64, 1111-1123.

Bard, P.Y. and Bouchon, M. (1980). Seismic response of sediment-filled valleys, Part 1: The case of incident SH waves, Bull. Seismol. Soc. Am. 70, 1263-1286.

Cabinet Office (2015): Report on Long-period Ground Motion Due to a Nankai Trough Megaquake, Committee for Modeling a Nankai Trough Megaquake, December 17, 2015, http://www.bousai.go.jp/jishin/nankai/nankaitrough_report.html, (in Japanese, last accessed, 2020/8/29).

Central Disaster Management Council, (2003): Strong motions and Tsunami heights, Figures and Tables, Vol.3, http://www.bousai.go.jp/kaigirep/chuobou/senmon/tounankai_nankaijishin/16/pdf/siryou3zuhyou_2.pdf (in Japanese, last accessed 2020/08/25).

Ito, E., Nakano, K, Nagashima, F., and Kawase H. (2020): A Method to Directly Estimate S-Wave Site Amplification Factor from Horizontal-to-Vertical Spectral Ratio of Earthquakes (eHVSRs), Bull. Seismol. Soc. Am. (Online only at present), 1–20, doi: 10.1785/0120190315.

Iwata, T. and Irikura, K. (1988): Source parameters of the 1983 Japan-Sea earthquake sequence, J. Phys. Earth, 36, 155-184.

J-SHIS (2020): Japan Seismic Hazard Information Station, NIED, Tsukuba, Japan, http://www.j-shis.bosai.go.jp/en/ (last accessed 2020/08/25)

Kamae, K. and Irikura, K. (1998): Source model of the 1995 Hyogo-ken Nanbu earthquake and simulation of near-source ground motion, Bull. Seism. Soc. Am., 88(2), 400–412, 1998.

Kamae, K. and Kawabe, H. (2004): Source model composed of asperities for the 2003 Tokachi-oki, Japan, earthquake (MJMA=8.0) estimated by the empirical Green's function method, Earth Planets Space, Vol. 56, 323–327.

Kawase, H. and Aki, K. (1989): A study on the response of a soft basin for incident S, P, and Rayleigh waves with special reference to the long duration observed in Mexico City, Bull. Seismol. Soc. Am., 79, 1361-1382, 1989.

Kawase, H. (2003): Site effects on strong ground motions, International Handbook of Earthquake and Engineering Seismology, Part B, W.H.K. Lee and H. Kanamori (eds.), Academic Press, London, 1013-1030.

Kawase, H. and Matsuo, H. (2004): Amplification characteristics of K-NET, KiK-NET, and JMA Shindokei network sites based on the spectral inversion technique, 13th World Conf. on Earthquake Engineering, Vancouver, Canada, Paper No. 454.

Kawase, H., Sánchez-Sesma, F.J., and Matsushima, S. (2011): The optimal use of horizontal-to-vertical spectral ratios of earthquake motions for velocity inversions based on diffuse field theory for plane waves", Bull. Seismol. Soc. Am., 101, 2001-2014.

Koketsu K., Miyake H., Suzuki H., (2012) Japan integrated velocity structure model version 1. Proceedings of the 15th world conference on earthquake engineering, Lisbon, Portugal, September, 24-28.

Kurahashi, S., and Irikura, K. (2013): Short-period source model of the 2011 Mw 9.0 off the Pacific coast of Tohoku earthquake, Bull. Seismol. Soc. Am., Vol.103, 1317-1393.

Mai, P.M. and Beroza, G.C. (2002): A spatial random field model to characterize complexity in earthquake slip, Journal of Geophysical Research, 107(B11), 2308, doi:10.1029/2001JB000588.

Miyakoshi, K. and Petukhin, A. (2005): Delineation of rupture velocity of heterogeneous source model extracted from source inversion results of inland earthquakes, Proc. of 2005 Japan Earth and Planetary Science Joint Meeting, May, 22-26, 2005, Chiba, Japan, S046P-002.

Morikawa, N. and Fujiwara, H. (2013): A new ground motion prediction equation for Japan applicable up to M9 mega-earthquake, J. Disaster Res., Vol. 8, No. 5, 878-888, doi:10.20965/jdr.2013.p0878.

Nagato, K and Kawase, H. (2004): Damage evaluation models of reinforced concrete buildings based on the damage statistics and simulated strong motions during the 1995 Hyogo-ken Nanbu earthquake, Earthq. Eng. and Struct. Dyn., Vol.33, No.6, 755-774.

Nagashima, F., Matsushima, S., Kawase, H., Sánchez-Sesma, F.J., Hayakawa, T., Satoh, T., and Oshima, M. (2014): Application of Horizontal-to-Vertical (H/V) spectral ratios of earthquake ground motions to identify subsurface structures at and around the K-NET Site in Tohoku, Japan, Bull. Seismol. Soc. Am., Vol. 104, No. 5, 2288–2302, doi: 10.1785/0120130219.

Nakano, K., Matsushima, S. and Kawase, H. (2015): Statistical properties of strong ground motions from the generalized spectral inversion of data observed by K-NET, KiK-net, and the JMA Shindokei Network in Japan, Bull. Seismol. Soc. Am., Vol.105, 2662-2680, doi:10.1785/0120140349.

Nakano, K. and Kawase, H. (2019): Source parameters and site amplifications estimated by generalized inversion technique: focusing on the 2018 Hokkaido Iburi-Tobu earthquake, Earth Planets Space, 71: 66, doi:10.1186/s40623-019-1047-1.

Nakano, K. (2020): Strong-motion prediction method based on the spectral inversion, Ph.D. Dissertation, Graduate School of Engineering, Kyoto University (in Japanese).

National Research Institute for Earth Science and Disaster Resilience (2019): NIED K-NET, KiK-net, National Research Institute for Earth Science and Disaster Resilience, doi:10.17598/NIED.0004

Renka, R. (1999) : Algorithm 790: CSHEP2D: Cubic Shepard Method for Bivariate Interpolation of Scattered Data, ACM Transactions on Mathematical Software, Vol. 25, No. 1, 70-73, doi:10.1145/305658.305737.

Rodgers, A., Petersson, N.A., Pitarka, A., McCallen, D., Sjogreen B., and Abrahamson, N. (2019): Broadband (0-5 Hz) fully deterministic three-dimensional ground motion simulations of a magnitude 7.0 Hayward Fault earthquake: Comparison with empirical ground motion models and 3D path and site effects from source normalized intensities, Seismol. Res. Lett., 90 (3), 1268-1284, doi: 10.1785/0220180261.

Satoh, T. (2004): Study on envelope model of ground motions based on inversion of group delay time and scattering theory, J. Struct. Constr. Eng., AIJ, No.586, 71-78, doi:10.3130/aijs.69.71_5 (in Japanese with English abstract).

Sekiguchi, H. and Yoshimi, M. (2010): Broadband Ground Motion Reconstruction for the Kanto Basin during the 1923 Kanto Earthquake, Pure and Applied Geophysics, doi:10.1007/s00024-010-0142-9.

Smith, F.H.W. and Wessel P.: Gridding with continuous curvature splines in tension, GEOPHYSICS, Volume 55, Issue 3, 1990, doi:10.1190/1.1442837.

Tsai, N.C. (1970): A note on the steady-state response of an elastic half-space, Bull. Seismol. Soc. Am., Vol.60, No. 3, 795-808.

Wessel, P., Smith, H.F.W., Scharroo, R., Luis, J.F., and Wobbe, F. (2013): Generic Mapping Tools: Improved version released, EOS Trans. AGU, 94, 409-410, 2013.

Yamaguchi, M. and Midorikawa, S. (2014): Empirical models for nonlinear site amplification evaluated from observed strong motion records, J. Japan Assoc. Earthq. Eng., Vol.14, No.1, 56-70, doi:10.5610/jaee.14.1_56 (in Japanese with English abstract).

(Received August 31, 2020)